



Structural origin of high catalytic activity for preferential CO oxidation over CuO/CeO₂ nanocatalysts with different shapes



Yu Xie^{a,1}, Jinfang Wu^{a,1}, Guojuan Jing^a, Hao Zhang^a, Shanghong Zeng^{a,*}, Xiaopeng Tian^a, Xinyue Zou^a, Jing Wen^a, Haiquan Su^a, Chuan-Jian Zhong^{b,*}, Peixin Cui^c

^a Inner Mongolia Key Laboratory of Chemistry and Physics of Rare Earth Materials, School of Chemistry and Chemical Engineering, Inner Mongolia University, Hohhot 010021, China

^b Department of Chemistry, State University of New York at Binghamton, Binghamton, NY 13902, United States

^c Key Laboratory of Soil Environment and Pollution Remediation, Institute of Soil Science, The Chinese Academy of Sciences, Nanjing 210008, China

ARTICLE INFO

Keywords:

Nanocrystal shapes
Oxygen vacancy
Metal-support interaction
Catalytic synergy
Preferential CO oxidation

ABSTRACT

Understanding how the shape of a nanocatalyst alters its catalytic performance is essential for the design of active catalysts at the nanoscale. This report describes novel findings of an investigation of CuO/CeO₂ nanocatalysts with different shapes for preferential CO oxidation (CO-PROX), aiming at unraveling the structural origin of the high catalytic activity. CuO/CeO₂ catalysts with a series of shapes, including octahedron, rod, cube, sphere and spindle morphologies, were synthesized by a combination of hydrothermal and impregnation methods. By probing the structure, elementary valence and reductivity of the catalysts using an array of techniques, an intriguing structure-activity synergy is revealed, pinning the origin of the highest catalytic activity to the intersection of the nanocrystal planes. The CuO/CeO₂ catalysts with spheres and spindles featuring exposed {111} and {002} crystal planes of CeO₂ were found to exhibit the lowest reaction temperature in terms of 50% CO conversion and a wider temperature window for the complete CO conversion in CO-PROX. The catalytic synergy reflects a combination of high surface area, reduced state of copper sites, high oxygen vacancies, as well as stronger interaction between CuO and CeO₂. This synergy was further substantiated by analysis of the results based on DFT calculation, showing that the oxygen vacancies were the highest at the intersection of {111} and {002} facets, but the lowest on CeO₂ {111} surface. The finding of {111} and {002} facets with an increased oxygen vacancy and a stronger metal-support interaction for improving the catalytic performance has important implications for designing facet-tunable nanocatalysts for efficient PROX.

1. Introduction

For proton exchange membrane fuel cells (PEMFCs), which effectively convert the chemical energy of hydrogen into electricity in stationary and mobile applications with high power density and reduced environmental pollution, the hydrogen fuel is usually generated by steam reforming, partial oxidation or auto-thermal reforming of hydrocarbons in combination with low-temperature water gas shift reaction [1]. It is critical to eliminate the traces of CO from hydrogen stream in order to avoid poisoning the Pt anode. CO preferential oxidation (CO-PROX) in H₂-rich stream has been considered as the most straightforward and effective method for CO elimination among different possible alternatives [2]. Catalysts based on the combination between copper and ceria constitute an economical choice in comparison with noble

metal catalysts (e.g., Au, Pt, Ru) [3–5]. The performance of CuO-CeO₂ catalysts is mainly linked to synergistic redox properties and interfacial interaction between copper and ceria [6,7]. Changing the geometrical shapes of the copper - ceria contact interface sites could adjust the key properties related to catalytic performance [8]. CeO₂ that possesses a cubic fluorite structure with three low-index planes may be prepared to produce different morphologies such as nanorods, nanocubes and nanotubes, which could tune the reactivity of supported copper species located at the interface perimeter. To date, a great deal of efforts has been placed on synthesizing CeO₂ containing different nanocrystal surfaces with uniform and controlled morphologies, but little has been established for correlating the shape morphologies with the catalytic properties.

The morphology of CeO₂ has been found to play an important role

* Corresponding author.

E-mail addresses: zengshanghong@imu.edu.cn (S. Zeng), cjzhong@binghamton.edu (C.-J. Zhong).

¹ These authors contributed equally to this work and should be considered co-first authors.

in CO-PROX reaction. For example, Au/CeO₂-rod catalysts were shown to exhibit the lowest apparent activation energy for CO oxidation compared with the Au/CeO₂-polyhedra and Au/CeO₂-cubes [9]. Similarly, compared the catalytic properties of Ag/CeO₂-nanorods (with exposed {110} and {100} planes) and nanocubes (enclosed with {100} planes) catalysts, Ag/CeO₂-nanorods were found to exhibit a higher oxygen vacancy concentration and stronger silver-ceria interaction than nanocubes [10]. Recently, CuO/CeO₂-rod and CuO/CeO₂-polyhedra were shown to exhibit a higher low-temperature catalytic oxidation activity, which is attributed to a higher content of the active species Cu⁺, stronger interaction and more oxygen vacancies on the surface [11]. Then poor performance of CuO/CeO₂-cube for CO-PROX was believed to result from weak interactions between copper and ceria with the exposure of {100} facets. Theoretical calculations over CuO/CeO₂ catalysts show that copper atoms on ceria {111} planes prefer to exhibit as Cu⁺, whereas they could be oxidized as Cu²⁺ on ceria {110} planes. CuO_x clusters on ceria {111} planes were easily reduced to Cu(I) species, which was shown to improve the catalytic reactivity [12]. The strength of interaction between copper and ceria with different exposed faces is intrinsically relevant to the catalytic performance. These prior studies have demonstrated the importance of nanocrystal planes of CuO-CeO₂ catalysts in CO-PROX reaction, but offered little on the exact origin of the increased catalytic activity.

In this work, we focus on a detailed investigation of CuO/CeO₂ nanocatalysts by comparing five different shapes, including octahedron, rod, cube, sphere and spindle morphologies, aiming at unraveling the structural origin of the high catalytic activity. These catalysts were synthesized by a combination of hydrothermal and impregnation methods. The surface sites and the interactions between copper oxide and ceria with different exposed faces enabled us to examine the nanocatalysts' facets in terms of oxygen vacancies and metal-support interaction for assessing the catalytic performance. To our knowledge, the comparison of the nanocatalysts with these different shapes in terms of the nanocrystal facet effect on the CO-PROX activity is the first attempt in probing the structural origin of the enhanced catalytic performance.

2. Experimental section

2.1. Catalyst preparation

All of the chemicals in our experiments were of analytical grade and used without further purification. Cerium nitrate hexahydrate (99.0%), copper nitrate (99.0%) and sodium hydroxide (96.0%) were purchased from Tianjin FengChuan Chemical Research Institute (Tianjin, China). Sodium phosphate (98.0%) was obtained from Tianjin Guangfu Fine Chemical Research Institute (Tianjin, China). Ethanol (99.7%), PVP and ethylene glycol were purchased from Tianjin FengChuan Chemical Research Institute (Tianjin, China).

2.1.1. Support preparation

CeO₂ supports with different morphologies were synthesized by a modified hydrothermal method [13,14]. CeO₂ octahedrons were prepared by the following steps. First, 8 mmol Ce(NO₃)₃·6H₂O and 0.08 mmol Na₃PO₄·12H₂O were dissolved in 64 mL deionized water and stirred for 1 h. The mixture was then poured into an 80 mL Teflon-lined stainless autoclave and heated at 160 °C for 24 h. After the hydrothermal treatment, the mixture was centrifuged and washed with deionized water and ethanol three times. Finally, the products were dried at 80 °C for 24 h and calcined at 600 °C for 5 h to obtain CeO₂ support with octahedron morphology.

CeO₂ rods and cubes were synthesized as below. First, 3.2 mmol Ce (NO₃)₃·6H₂O and 0.384 mol NaOH were dissolved in 64 mL deionized water and stirred for 30 min. Then, the mixture was poured into an 80 mL Teflon-lined stainless autoclave and heated at different temperature for 24 h (rods: 100 °C; cubes: 180 °C). After the hydrothermal treatment, the mixture was centrifuged and washed with deionized

water and ethanol three times. Finally, the products were dried at 80 °C for 24 h and calcined at 600 °C for 5 h to obtain CeO₂ support with rod and cube morphologies.

CeO₂ spheres were prepared by a previously reported method [14]. 4.6 mmol Ce(NO₃)₃·6H₂O and 0.8 g PVP were dissolved in 56 mL of ethylene glycol. 8 mL deionized water was added to the above mixture and stirred for 30 min. Then, the mixture was poured into an 80 mL Teflon-lined stainless autoclave and heated at 160 °C for 24 h. After the hydrothermal treatment, the mixture was washed with deionized water and ethanol several times. Finally, the products were dried at 80 °C overnight and calcined at 600 °C for 5 h to obtain CeO₂ support with sphere morphology.

CeO₂ spindles were synthesized by the following procedure. First, 1.92 mmol Ce(NO₃)₃·6H₂O and 5.12 mmol urea were dissolved in 64 mL deionized water and stirred for 30 min. Then, the mixture was poured into an 80 mL Teflon-lined stainless autoclave and heated at 80 °C for 8 h. After the hydrothermal treatment, the mixture was collected and washed with deionized water and ethanol three times. Finally, the products were dried at 80 °C for 24 h and calcined at 600 °C for 5 h to obtain CeO₂ support with spindle morphology.

2.1.2. Catalyst preparation

The CuO/CeO₂ catalysts were prepared by equal volume impregnation method. The as-synthesized CeO₂ supports were impregnated in a solution of copper nitrate. The molar ratio of CeO₂ to CuO was 5. After 24 h impregnation, the samples were dried at 60 °C overnight for 24 h in air, and then calcined at 400 °C for 2 h in a muffle furnace.

2.2. Catalyst characterization

The morphologies of the as-prepared CeO₂ supports were characterized by field-emission SEM performed on a Hitachi S-4800 scanning electron microscope with an accelerating voltage 10.0 kV. The CeO₂ supports with different morphologies were coated with a thin layer of Au before the measurement.

Transmission electron microscopy (TEM) measurements were operated on a FEI Tecnai G² F20 S-Twin transmission electron microscope at 200 kV. The samples were suspended in ethanol solution using an ultrasonic bath for 30 min. One drop of the suspension was cast on a copper grid for the TEM sample preparation.

Powder X-ray diffraction (XRD) patterns of the samples were recorded on a PANalytical X' pert PRO diffractometer with Cu K α radiation ($\lambda = 0.1542$ nm) operating at 100 mA and 40 kV. Bragg's angles were scanned in the range of 2θ between 20 and 80°. The average crystallite sizes were estimated from the Scherrer's equation.

Brunauer-E Emmet-Teller (BET) surface area and pore volume of the samples were determined by measuring N₂ adsorption-desorption isotherms at liquid nitrogen temperature (-196 °C) using a Micromeritics ASAP2020 adsorption apparatus. The samples were degassed under a vacuum of 10^{-5} Torr for 12 h at 200 °C.

X-ray photoelectron spectroscopy (XPS) measurements were performed on a Thermo ESCALAB 250XI spectrometer with a monochromatic Al K α (1486.6 eV) radiation source. During data processing of XPS spectra, the charging shift was calibrated using C 1s value of adventitious carbon at binding energy 284.8 eV.

UV-vis diffuse reflectance spectra of the samples were recorded on a UV-vis spectrophotometer (U3900, Hitachi) with an integrating sphere attachment within the range of 200–800 nm. BaSO₄ was used as the reflectance standard. From UV-vis spectra, the band gap was estimated by plotting $[(F(R)\hbar\nu)^{1/2}]$ against energy. The linear part of the curve further was extrapolated to $[(F(R)\hbar\nu)^{1/2}] = 0$ for determining the band gap.

H₂ temperature-programmed reduction (TPR) was conducted on a Micromeritics Apparatus (AutoChem II 2920) to examine the redox behavior of the samples. The gas was 10% H₂/Ar mixture and the flow rate of gas was 50 mL·min⁻¹. Approximately 100 mg sample was placed

on top of some silica wool in a quartz reactor. Before reduction, the sample was pretreated at 200 °C for 1 h in a N₂ stream in order to remove the contaminants, after which it was cooled to room temperature. The H₂/Ar mixture was switched on and the sample was heated with a heating rate of 10 °C min⁻¹. The reaction was performed from room temperature to 800 °C.

The X-ray absorption fine structure (XAFS) spectra at Cu K-edge were collected at the beamline BL 14W1 of the Shanghai Synchrotron Radiation Facility (SSRF). The typical energy of the storage ring was 3.5 GeV in the top-up mode with an electron current of ~220 mA. The white light was monochromatized by a Si (111) double-crystal monochromator and calibrated with a Cu foil (K-edge at 8979 eV). The XAFS spectra were recorded in fluorescence mode with a Lytle detector oriented at 90° to the incoming beam. The X-ray absorption near edge structure (XANES) was obtained by background subtraction and normalization. In the extended X-ray absorption fine structure (EXAFS) part, Fourier transformed (FT) data were analyzed in R-space by using the first-shell approximation model. The amplitude reduction factor (S_0^{-2}) was estimated to be 0.916 according to the results of the copper foil with the first two coordination numbers (CN) set as 12 and 6, and then applied to all other samples. The coordination parameters of sorption samples were obtained by fitting the experimental peaks with theoretical amplitude.

To further investigate the second-shell backscattering atoms and detect light and heavy scatters at similar distances, wavelet transform (WT) analysis was employed by using qualitative analysis, which focused on the nature of the backscattering atoms as well as the bond lengths owing to the fine resolution in both wavenumbers k and radial distribution function R , and complemented the limitation of FT analysis. The Morlet wavelet was chosen as basis mother wavelet and the parameters ($\eta = 9$, $\sigma = 1$) were used for a better resolution in the wave vector k .

2.3. Computational modeling

Ab initio calculations were performed by density functional theory (DFT) as implemented in Dmol3 program coming as a part of Materials Studio software. Herein a polyhedral Ce₆₀O₁₂₀ cluster was built to model different facets and their interfaces (Scheme S1, Supporting Information (SI)). The DFT calculations were carried out with the Perdew-Wang (PW91) function of generalized gradient approximation (GGA) using the polyhedral model of Ce₆₀O₁₂₀ in Scheme S1. The localized double numerical basis sets with d-functions (DND) were employed for valence orbitals, and effective core potential (ECP) was used to account for the core electrons. The spin-unrestricted approach was used to calculate the adsorption properties. The convergence tolerance of the maximum force was 2×10^{-3} Ha/Å and the energy charge was 1×10^{-5} Ha. To reveal the dependence of CO preferential oxidation on CeO₂ support, the energy for the surface oxygen vacancy formation (E_{vac}) was calculated by removing an oxygen atom from CeO₂ surfaces. E_{vac} was calculated as follows:

$$E_{\text{vac}} = E_{\text{Ce}_{60}\text{O}_{119}} + \frac{1}{2}E_{\text{O}_2} - E_{\text{Ce}_{60}\text{O}_{120}} \quad (1)$$

Where $E_{\text{Ce}_{60}\text{O}_{119}}$, E_{O_2} and $E_{\text{Ce}_{60}\text{O}_{120}}$ are the energy for the defective cluster, the gas-phase O₂ molecule, and the intact cluster, respectively.

The adsorption of CO on CeO₂ surface was also investigated, and the adsorption energy (E_{ads}) was obtained as follows:

$$E_{\text{ads}} = E_{\text{CO-cluster}} - E_{\text{cluster}} - E_{\text{O}_2} \quad (2)$$

Where $E_{\text{CO-cluster}}$ and E_{cluster} are total energy of the CO-CeO₂ cluster complex and the isolated CeO₂ cluster.

2.4. Catalytic activity measurement

Catalytic activity of the catalysts was measured in a tubular quartz

micro-reactor. The gas feed contained 1.0 vol% CO, 1.0 vol% O₂ and 50.0 vol% H₂ with N₂ as balance gas. The catalysts were grinded and sieved by a 200-mesh sieve in order to ensure the elimination of external mass transfer. The catalysts were then mixed with quartz sand that had equal pellet size and amount. The space velocity was 40,000 mL g_{cat}⁻¹ h⁻¹, and the temperature was from 35 to 215 °C. The products and reactants were analyzed using an online GC-2014C gas chromatograph equipped with a thermal conductivity detector (TCD). The CO, O₂ and N₂ were separated by a 5 Å molecular sieve column, and CO₂ was separated by a TDX column. The conversion of CO (C_{CO}) and O₂ (C_{O2}) and the selectivity of CO₂ (S_{CO2}) were defined according to Eqs. (3)–(5), respectively [15].

$$C_{\text{CO}} (\%) = ([\text{CO}]_{\text{in}} - [\text{CO}]_{\text{out}}) / [\text{CO}]_{\text{in}} \times 100 \quad (3)$$

$$C_{\text{O}_2} (\%) = ([\text{O}_2]_{\text{in}} - [\text{O}_2]_{\text{out}}) / [\text{O}_2]_{\text{in}} \times 100 \quad (4)$$

$$S_{\text{CO}_2} (\%) = C_{\text{CO}} / 2C_{\text{O}_2} \times 100 \quad (5)$$

3. Results and discussion

3.1. Morphological and structural characterizations

3.1.1. Comparison of morphologies of nanocrystals with different shapes

Different morphologies of CeO₂ supports were successfully synthesized by the modified hydrothermal method (Fig. 1). As shown in Fig. 1A, the edge length of the octahedrons changes from 110 to 280 nm. The rods feature 8–10 nm in diameter and 40 to 200 nm in length (Fig. 1B). The bright spots on the surface of rods indicate the presence of lattice defects [13]. Fig. 1C displays nonuniform cubes with sides ranging from 20 to 100 nm. Fig. 1D shows uniform spheres with a size of ~180 nm. The spheres are composed of closely packed CeO₂ nanoparticles with a diameter of about 8 nm as primary building blocks. Another shape of the supports involves large spindles with a size of ~8 μm, as shown in Fig. 1E. Understanding of how the different shapes of CeO₂ supports would influence the structural and electronic properties of the metal nanoparticles dispersed on the supports is an important aspect of our investigation in this work.

Fig. 2 shows a representative set of TEM images and corresponding FFT patterns of the CuO/CeO₂ catalysts. It can be observed that the respective morphologies of the differently-shaped CeO₂ supports remain after loading CuO. The lattice fringe for the CuO was not identifiable, likely reflecting high dispersion of CuO over the CuO/CeO₂ catalysts. Remarkably, CeO₂ octahedrons preferentially expose {111} planes, which are the thermodynamically most stable crystal planes (Fig. 2A). Similarly, CeO₂ rods expose a large amount of {111} planes with a growth direction along {022} planes, with a small amount of {002} planes observable in the HRTEM image and FFT pattern (Fig. 2B). As seen from Fig. 2C, CeO₂ cubes predominantly expose {002} crystal planes with 0.277 nm for the interplanar spacing. In addition, the exposed planes of CeO₂ nanospheres and spindles are {111} and {002} crystal planes, as observed in Fig. 2D and Fig. 2E. It is worth mentioning that there are some voids in the overall morphology for CuO/CeO₂ (spheres), indicating that the CeO₂ particles with a crystallite size of 8 nm are loosely arranged into spherical shapes.

It is well known that the formation of oxygen vacancies on CeO₂ is strongly surface sensitive, implying that different exposed facets of the CeO₂ supports could produce different lattice defects. This would result in different structures of oxygen vacancies including small or large vacancy clusters or vacancy lines [16]. The formation energy of oxygen vacancies on {111} crystal facet, which is the most compact and less prone to accommodate a vacancy defect, is higher than those on other crystal planes. High-energy {002} and {022} planes have more oxygen vacancies and can promote activation of molecular oxygen [17]. This assessment is supported by a report of Trovarelli and Llorca, showing that the exposure of specific facets can increase or decrease metal-

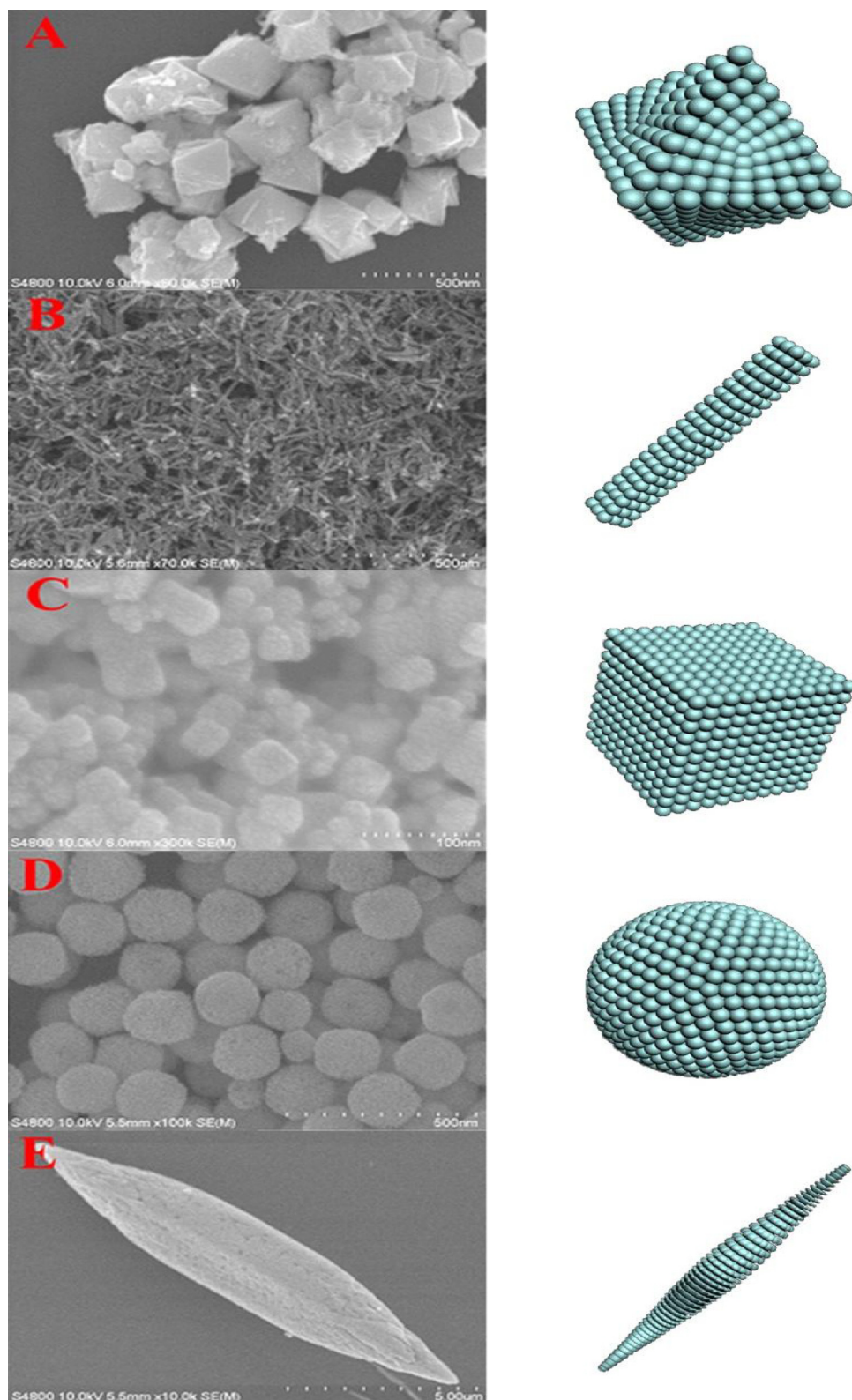


Fig. 1. SEM images of the CeO₂ supports with different shapes: (A) octahedrons, (B) rods, (C) cubes, (D) spheres and (E) spindles.

support interaction and surface oxygen reactivity which play crucial roles in the activity and selectivity [18].

The elemental distribution across each of the different shapes was further substantiated by EDS mapping of the elemental composition in the CuO/CeO₂ catalysts (Fig. 3). It is evident that CuO species are not only highly dispersed but also homogeneously dispersed on the CeO₂

supports. There are the round-shaped particles on the edge in the EDS mapping of CuO/CeO₂ (spindles), which are assigned to CuO and CeO₂ combined with the analyses from Fig. 1E.

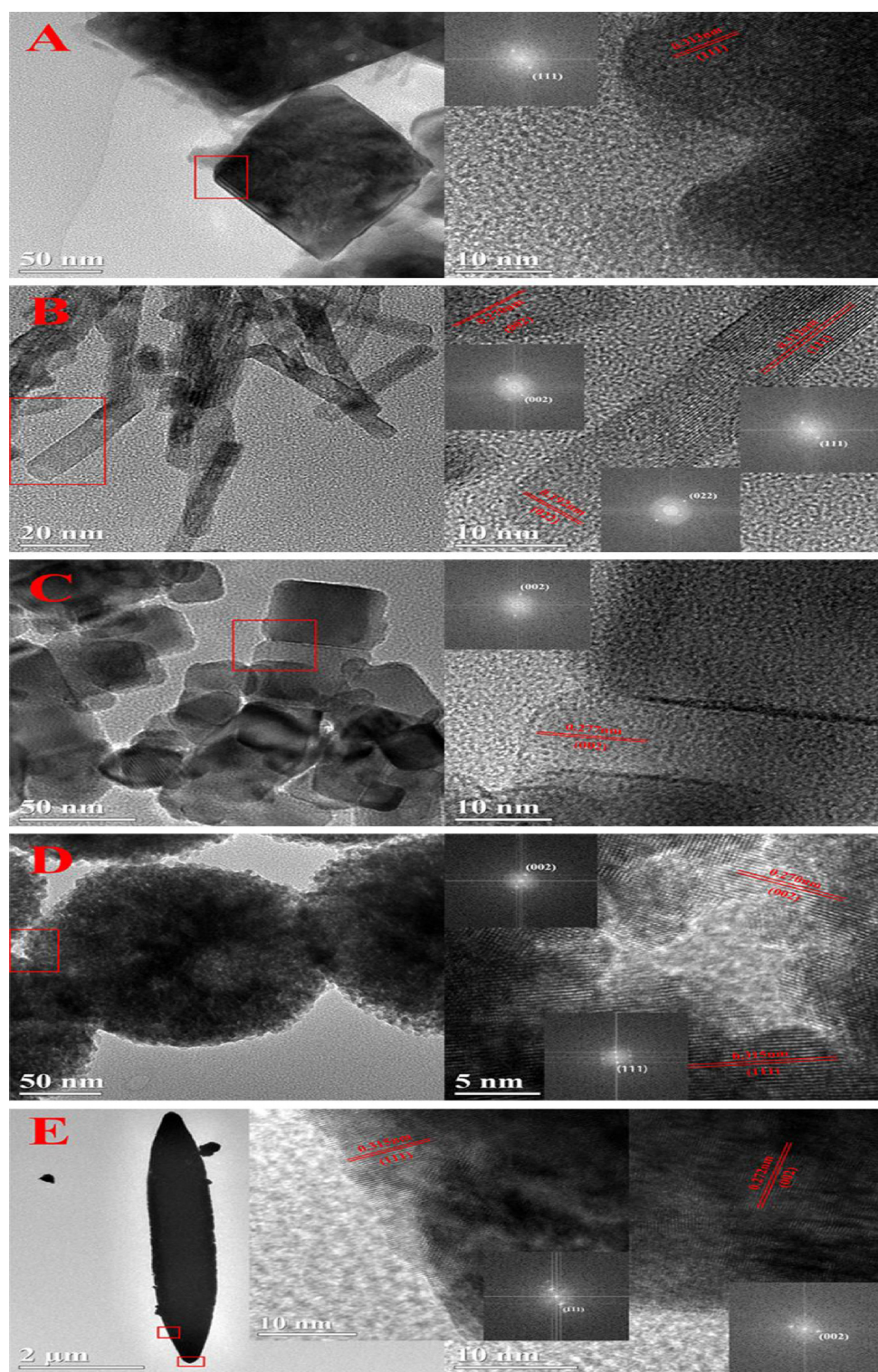


Fig. 2. TEM images (left panels) and the corresponding HRTEM images (right panels) and FFT pattern (inset) for the CuO/CeO₂ catalysts with different shapes: (A) octahedrons, (B) rods, (C) cubes, (D) spheres, and (E) spindles.

3.1.2. Comparison of structure and surface properties of nanocrystals of different shapes

Fig. 4 shows a representative set of XRD patterns for the CuO/CeO₂ catalysts. Figure S1 (SI) also display XRD patterns of the CeO₂ supports with different shapes. The diffraction peaks are well-defined and match the standard diffraction data of fluorite-type CeO₂ (PDF#98-005-4356). For CuO/CeO₂ catalysts, the small peaks at 35.6° and 38.7° could be indexed to CuO (PDF#98-005-9563). The weak diffraction peaks for

CuO indicate that CuO is highly dispersed on the CeO₂ supports with different morphologies. It is consistent with the results of EDS analyses. In addition, the peak width of the XRD diffractions is related to the crystallinity. XRD patterns of octahedrons and cubes display sharp peaks of CeO₂ with the high intensity, suggesting that CeO₂ has a good crystallinity in these two samples.

The lattice parameter and mean crystallite size of CeO₂ were estimated based on Bragg's equation and Scherrer's equation, respectively.

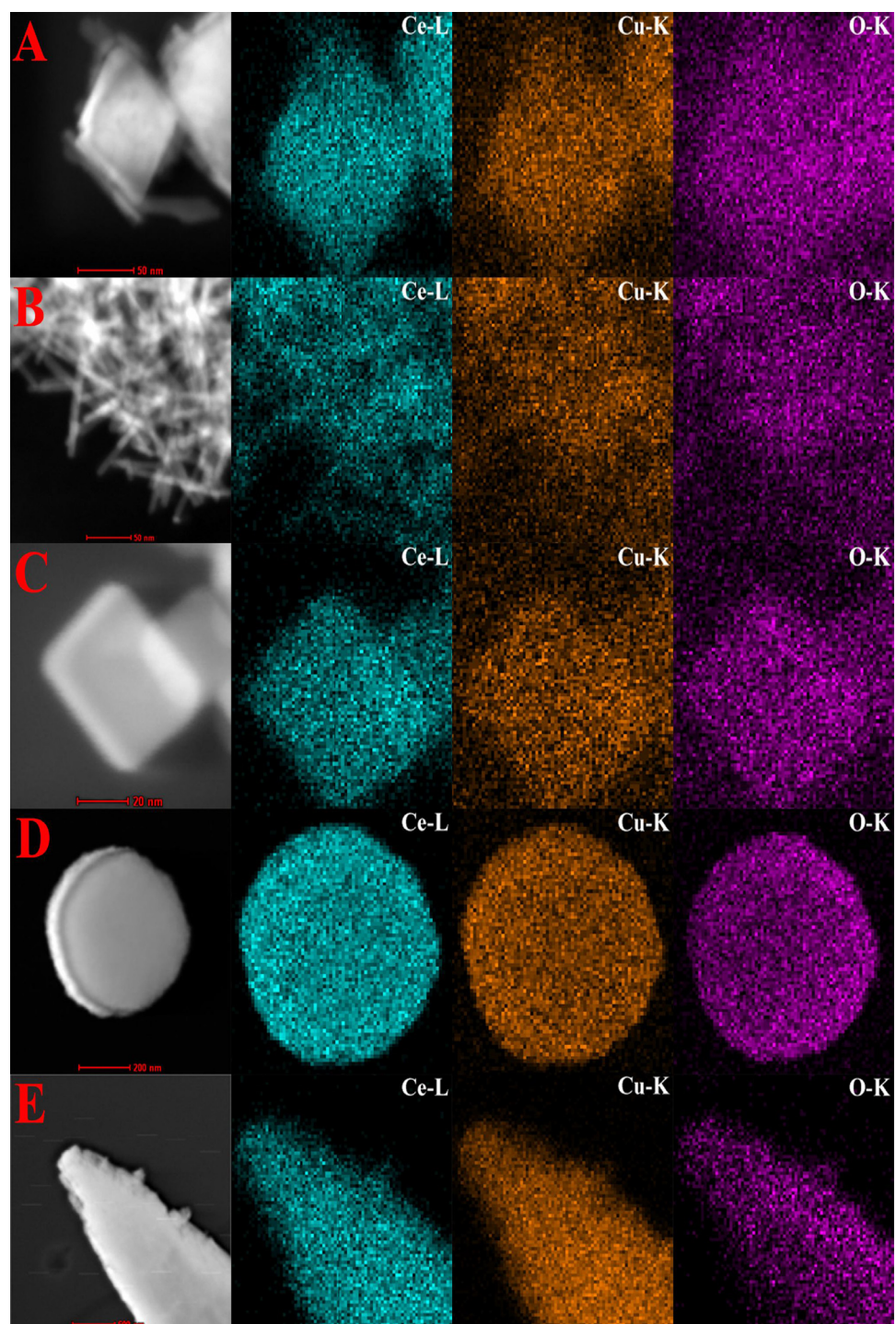


Fig. 3. EDS mapping of the CuO/CeO₂ catalysts with different shapes: (A) octahedrons, (B) rods, (C) cubes, (D) spheres, and (E) spindles.

As shown in Table 1, the lattice parameter of CeO₂ in the CuO/CeO₂ (rods) CuO/CeO₂(spindles) catalysts is smaller than that in pure CeO₂ (0.5411 nm) [19], suggesting that copper ions with smaller ionic radius than Ce⁴⁺ incorporate into the CeO₂ lattice forming lattice defects. The active oxygen species are easily generated on the highly defective and faceted surfaces. The spheres appear to exhibit the highest lattice parameter (0.5414 nm) due to high concentration of Ce³⁺ defects on the surface (XPS results), which decreases the electrostatic forces and results in an increase of lattice parameter. The mean crystallite size is ranked in the order of cubes > octahedrons > rods > spindles > spheres, which is in agreement with the crystallinity of CeO₂ supports.

The results suggest that small CeO₂ nanoparticles show high oxygen storage capacity (OSC) because they could modify the oxygen vacancy on ceria surface [20,21].

N₂ adsorption-desorption isotherms for the CuO/CeO₂ catalysts were displayed in Fig. 5. It can be observed that the isotherms are typical type-IV isotherms according to five types of isotherms from Brunauer-Deming-Deming-Teller (BDDT) pore model [22]. The CuO/CeO₂ catalysts with octahedron, rod and cube morphologies exhibit type H3 hysteresis loops in the relative pressure (P/P₀) range from 0.6 to 1.0, and their pore size distribution curves (see Figure S2, SI) show a wide range of pore sizes from micropore to mesopore [23]. The CuO/CeO₂

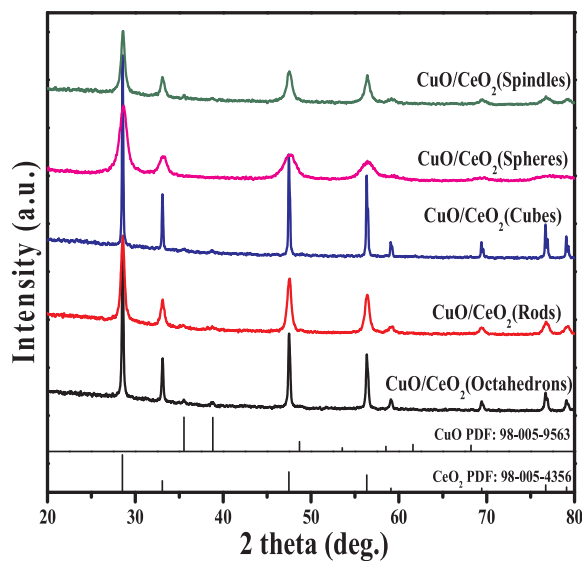


Fig. 4. XRD patterns of the CuO/CeO₂ catalysts with different support shapes: octahedrons, rods, cubes, spheres and spindles.

Table 1
Structural and morphological properties of the CuO/CeO₂ catalysts.

Catalyst	CeO ₂ cell parameter (nm) ^a	Crystallite size (nm) ^b	S _{BET} (m ² g ⁻¹)	Pore volume (cm ³ g ⁻¹)
CuO/CeO ₂ (octahedrons)	0.5411	48.4	14.3	0.08
CuO/CeO ₂ (rods)	0.5410	15.3	40.0	0.19
CuO/CeO ₂ (cubes)	0.5411	78.1	7.2	0.05
CuO/CeO ₂ (spheres)	0.5414	8.3	108.3	0.06
CuO/CeO ₂ (spindles)	0.5410	15.0	42.1	0.05

^a Calculated from XRD data using Bragg's equation for a cubic cell.

^b Calculated from XRD data using Scherrer's equation according to the [111] diffraction peaks of CeO₂.

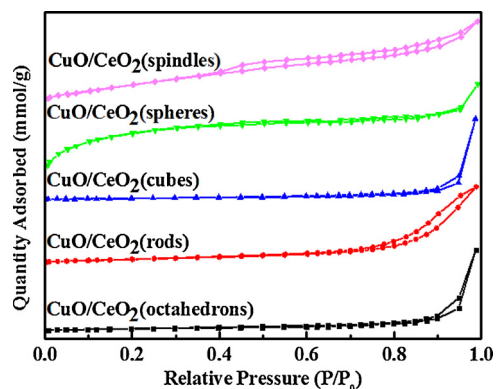


Fig. 5. N₂ adsorption-desorption isotherms of the CuO/CeO₂ catalysts with different support shapes: octahedrons, rods, cubes, spheres and spindles.

catalysts with spindle and sphere morphologies exhibit type H4 hysteresis loops in the relative pressure (P/P₀) range from 0.4 to 1.0, characteristic of microporous solids. Among them, the sphere catalyst displays uniform pore size distribution and the most probable peak appears at about 1 nm in Figure S2. Moreover, as seen in Table 1, the sphere catalyst has the largest BET surface area of 108.3 m²/g. The order of BET surface areas, spheres > spindles > rods > octahedrons > cubes, is the exact opposite of the order of the corresponding mean crystallite sizes. Large BET surface area is favorable for oxygen storage capacity (OSC) of ceria because OSC takes place not

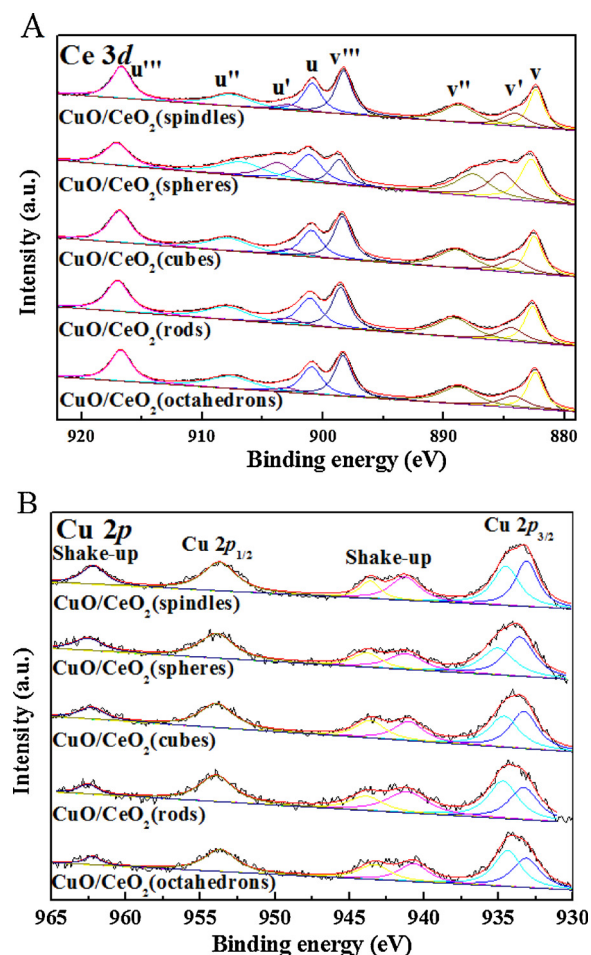


Fig. 6. XPS spectra of the CuO/CeO₂ catalysts with different support shapes in the binding energy regions of Ce 3d (A) and Cu 2p (B).

only on the surface but also in the bulk. Indeed, surface area of rods is generally larger than that observed in cubes [24,25]. It is evident that the morphologies and sizes of ceria have a great influence on the BET surface area of catalysts.

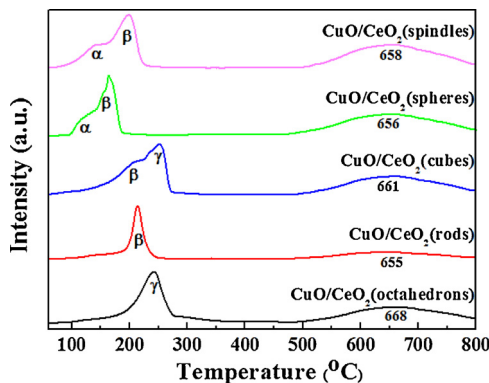
The surface composition and valence state of Cu and Ce were examined by XPS analysis (Fig. 6). The spectra for the Ce 3d region were deconvoluted into eight peaks with the assignments defined in Fig. 6A. The Ce 3d spectra are composed of two-group spin orbitals of overlapping peaks labeled as u (u-u'') for 3d_{3/2} and v (v-v'') for 3d_{5/2}. Among them, the u' (903.0 eV) and v' (884.2 eV) peaks were assigned to Ce³⁺, and the other six peaks corresponded to Ce⁴⁺ states. The surface relative amount of Ce³⁺, shown as Ce³⁺/Ce_{total} in Table 2, can be calculated by considering the relative integrated areas of the corresponding peaks and the total Ce 3d region [26–28]. The Ce³⁺ values are in the range of 10.2%–11.6% except for the sphere catalyst (23.7%). The high concentration of Ce³⁺ defects on the surface may be attributed to small particle size of ceria in the sphere catalyst, which has a greater ability to reduce copper oxides and form Cu⁺ species that are active sites for CO oxidation [29,30]. This process can be expressed as Cu²⁺ + Ce³⁺ → Cu¹⁺ + Ce⁴⁺.

Fig. 6B shows the Cu 2p core level spectra of the CuO/CeO₂ catalysts. There are two characteristic peaks for Cu 2p_{3/2}, namely, reduced Cu⁺ state centered at about 932.5 eV and Cu²⁺/CuO species centered at 933.8 eV with broad satellite peaks around 940–947 eV [31,32]. It is generally accepted that the degree of reduction of copper species can be calculated by the ratio of intensities of satellite peaks to those of main peaks, which is defined as I_{sat}/I_{main} ratio (Table 2), e.g., 0.57 for Cu²⁺ species. The lower I_{sat}/I_{main} ratio corresponds to a higher amount of

Table 2

Comparison of the surface properties and band gaps of the supports and catalysts.

Sample	Ce ³⁺ /Ce _{total} ^a	I _{sat} /I _{main} ^a	Cu/Ce surface ratio ^a	O _{latt} /O _{latt} + O _{ad} ^a	Band gap (eV) ^b CeO ₂ supports	Band gap (eV) ^b CuO/CeO ₂ catalyst
CuO/CeO ₂ (octahedrons)	10.2	0.55	0.36	0.23	3.25	3.19
CuO/CeO ₂ (rods)	11.5	0.55	0.40	0.62	3.16	3.08
CuO/CeO ₂ (cubes)	11.5	0.55	0.47	0.54	3.27	3.18
CuO/CeO ₂ (spheres)	23.7	0.47	0.66	0.75	3.10	2.98
CuO/CeO ₂ (spindles)	11.6	0.50	1.07	0.65	3.10	3.04

^a Calculated from XPS Spectra.^b Calculated from UV-vis Spectra (see Figure S4 in SI) [38–40].**Fig. 7.** H₂-TPR profiles of the CuO/CeO₂ catalysts with different support shapes: octahedrons, rods, cubes, spheres and spindles.

reduced copper species [33]. The reduced copper species that has a strong interaction with ceria exist in all the catalysts, which were proposed as the main active sites of Cu-O-Ce for CO PROX [34,35]. Clearly, the CuO/CeO₂ (spheres) exhibits a maximum for the reduced copper species. The amount of reduced copper species are in order of spheres > spindles > rods = cubes = octahedrons, which is consistent with the concentration of Ce³⁺ defects on the surface.

As listed in **Table 2**, the Cu/Ce surface ratios are high than the preparation one (0.2), indicating that CuO is highly dispersed on the CeO₂ supports with different morphologies. It is accordant with the analyses of EDS and XRD measurements. In the O 1s core level spectra as shown in Figure S3 (see SI), the peaks centered at 529.4 eV are assigned to the lattice oxygen (O_{latt}), and those centered at 531.4 eV correspond to the surface hydroxyl or carbonate chemisorbed oxygen species (O_{ad}) [36,37]. The O_{latt} quantity in the CuO/CeO₂ catalysts shows an order of spheres > spindles > rods > cubes > octahedrons.

For band gap of the CeO₂ supports and CuO/CeO₂ catalysts in **Table 2** (Figure S4), the CeO₂ supports with different morphologies exhibit different band gap energies, reflecting the differences in the coupling state of electron spin-orbit between Ce 3d and O 2p [41]. For CuO/CeO₂ catalysts, the introduction of copper oxides reduces the band gap in contrast to the CeO₂ supports. The CuO/CeO₂ sphere catalyst has the lowest band gap in the as-prepared samples which exhibits the order of spheres < spindles < rods < cubes < octahedrons. The shrinkage of band gap reflects the presence of close interaction of Cu-Ce species because CuO electronic levels fall the band gap between ceria valence and conduction band [42–44]. It is reported that Cu supported over ceria nanorods is more active for carbonate hydrogenation than that over CeO₂ supports with cube and polyhedra morphologies due to a stronger interaction between metal and support. This leads to a balanced distribution of copper species, which improves reducibility of the catalysts [45]. It is evident that there is a stronger interaction between Cu and CeO₂ when Cu is supported on ceria spheres and spindles in comparison with ceria rods. Therefore, as shown by TPR analysis next, CuO on ceria spheres and spindles is more easily reduced than that

on the other three supports, indicating that the redox behavior of the catalysts correlated well with the interaction between Cu and CeO₂.

3.2. Determination of catalytic properties for CO-PROX

3.2.1. Surface interaction

The profile of pure CuO displays single reduction peak at 299 °C (Figure S5). Figure S6 displays H₂-TPR profiles of the CeO₂ supports with different shapes. H₂-TPR profiles of CeO₂ generally contain two reduction peaks, corresponding to the mechanism of two-step reduction [46]. The low-temperature reduction peaks at about 550 °C were the reduction of surface-capping Ce⁴⁺, and the high-temperature peaks at near 800 °C were assigned to the reduction of bulk ceria. It can be seen from Figure S6 that the CeO₂ supports with rods, spheres and spindles shapes have lower reduction temperatures compared with those with octahedrons and cubes morphology.

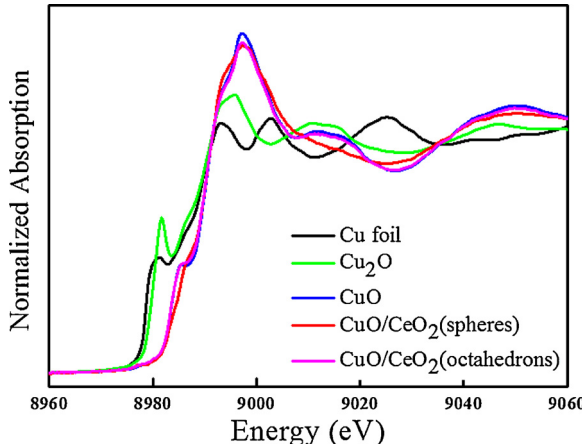
The H₂ temperature programmed reduction (H₂-TPR) profiles of the CuO/CeO₂ catalysts with different morphologies are shown in **Fig. 7**. There are three main peaks at 150 °C (peak α), 200 °C (peak β) and 250 °C (peak γ). Peak α was assigned to the reduction of the highly dispersed CuO_x species which interact strongly with the ceria. Peak β corresponds to the reduction of CuO_x species which interact weakly with the ceria. Peak γ was attributed to the reduction of bulk CuO [47].

It can be observed that there are two peaks (α and β) in the profiles of the CuO/CeO₂ catalysts with sphere and spindle morphologies. For CuO/CeO₂(cubes), β and γ peaks can be seen in the profile. However, there is only one peak in the profiles of CuO/CeO₂ catalysts with rod and octahedron morphologies. β peak appears in the profile of CuO/CeO₂(rods), and γ peak can be seen in the CuO/CeO₂(octahedrons). As shown in **Table 3**, the hydrogen consumption of the CuO/CeO₂ catalysts with sphere and spindle morphologies is similar (α and β peaks). For CuO/CeO₂(cubes), the consumption ratio of β peak is much larger than one of γ peak. The hydrogen consumption of CuO/CeO₂(rods) and CuO/CeO₂(octahedrons) only corresponds to β peak and γ peak, respectively. It suggests that the redox activity of copper oxides can be adjusted by synthesizing the CeO₂ supports with different exposed planes, and their influence on the catalytic performance is directly related to the redox behavior of copper oxides. As stated earlier, CeO₂ spheres and spindles expose {111} and {002} crystal faces, and CuO_x species interacting with ceria were easily generated when these two faces coexisted on ceria. For CuO/CeO₂(spheres), it has the lowest reductive temperature for copper oxides, which could also be attributed to the smallest crystallite size of CeO₂ and the largest BET surface area. Only bulk CuO exists in the profile of CuO/CeO₂(octahedrons) when only {111} crystal face is exposed. Clearly, the coexistence of crystal faces are more beneficial to form the CuO_x species interacting with the ceria, and easier removal of oxygen takes place at the intersection sites between {111} and {002} facets. In addition, the peaks at about 650 °C were assigned to the reduction of bulk ceria. The reductive temperature for bulk ceria in the catalysts is lower than in pure ceria (Figure S6), indicating that the loading of CuO species promotes the reduction of ceria [48].

Table 3

Summary of TPR results, concentration of oxygen vacancies and catalytic activities.

Catalyst	$\alpha(\%)^a$	$\beta(\%)^a$	$\gamma(\%)^a$	Exposed planes	$[V_O]^b$	$T_{50\%}^c$ (°C)	TOF(s ⁻¹) ^c	Temperature window (°C)
CuO/CeO ₂ (octahedrons)	–	–	100	{111}	2.55	155	0.18	195–215
CuO/CeO ₂ (rods)	–	100	–	{111} and less{002}	2.88	83	0.63	135–175
CuO/CeO ₂ (cubes)	–	75.1	24.9	{002}	2.88	103	0.20	155–195
CuO/CeO ₂ (spheres)	41.3	58.7	–	{111} and {002}	5.93	69	1.35	95–195
CuO/CeO ₂ (spindles)	41.7	58.3	–	{111} and {002}	2.90	74	1.04	115–215

^a Calculated from TPR data.^b Calculated from the equation of $[V_O] = 1 - (3[Ce^{3+}] + 4[Ce^{4+}]) / 4$.^c Calculated at 75 °C reaction temperature.**Fig. 8.** XANES spectra of CuO/CeO₂ (spheres) and CuO/CeO₂ (octahedrons) catalysts.

3.2.2. Fine structure

The XAFS technique was used to further analyze electronic structure of the copper species on ceria, which can help understand the detailed structure correlated with activity. The XANES spectra for Cu K edge in both spheres and octahedrons (Fig. 8) show the similar absorption edge with CuO in the range of 8960–9000 eV, indicating the presence of Cu²⁺. However, the XANES spectra for CuO/CeO₂ (spheres) in the range of 9010–9020 eV exhibit different line shape from CuO, demonstrating the coexistence of Cu²⁺ and other copper species.

The related EXAFS of Cu K edge (Figure S7 and Table S1, SI) exhibit significantly different peaks in the range of 2.1–3.3 Å labeled with blue dot line frame for CuO/CeO₂ (spheres) and CuO/CeO₂ (octahedrons), however, it is difficult to distinguish the coordination atoms because Cu and/or Ce have similar coordination bond distance. Therefore, wavelet transform (WT) analysis was employed to provide 3D image for the part of EXAFS blue frame, as shown in Fig. 9. It confirms that Cu²⁺ species is dominant in octahedrons, which has almost the same coordination structure as that of CuO. For spheres, the coordination structure shows significant difference from that in CuO and Cu₂O, suggesting the presence of Cu²⁺ and Cu⁺ species in agreement with XPS analysis. In a word, the spheres with {111} and {002} planes contain more low valence states of copper related to the activity of catalyst in comparison with the octahedrons with {111} plane. And the valence state of copper species is a critical factor to determine catalytic activity.

3.2.3. Catalytic activity

Fig. 10 shows a typical set of catalytic performance test results for preferential oxidation of CO over the CuO/CeO₂ catalysts. The experiments were carried out by using a synthetic gas (1.0% CO, 1.0% O₂, 50.0% H₂ and N₂ balance) in the 35–215 °C temperature range. Table 3 lists the temperatures corresponding to 50% CO conversion ($T_{50\%}$), TOF and the temperature window for complete CO conversion. It can be

observed that the as-prepared five catalysts with different morphologies display different catalytic performances. As seen in Table 3, the CuO/CeO₂(spheres) and CuO/CeO₂(spindles) exhibit lower temperatures for 50% CO conversion, higher TOF and a wider temperature window for complete CO conversion than the other three samples.

The results show that the catalytic activity for the CuO/CeO₂ catalysts is in the order of spheres > spindles > rods > cubes > octahedrons. As seen in Table 3, the CeO₂ spheres and spindles expose {111} and {002} crystal planes, and there is a large amount of {111} planes and a small amount of {002} planes for CeO₂ rods. It appears that the coexistence of {111} and {002} crystal planes on ceria is in favor of a higher catalytic activity. The finding is further supported by the fact that the CuO/CeO₂(cubes) which exposes {002} crystal planes and CuO/CeO₂(octahedrons) with exposed {111} facets display lower catalytic activity than the other three samples. The CeO₂ {111} crystal planes in the spheres facilitate the formation of Cu⁺ during the process of Cu²⁺ + Ce³⁺ → Cu¹⁺ + Ce⁴⁺, which is key active component in PROX reaction [49,50]. In contrast, the CuO/CeO₂(octahedrons) that only exposes {111} facets of ceria presents the lowest catalytic activity. Therefore, the effect of combination of {111} and {002} crystal planes should be taken into account when analyzing the crystal facet effect of ceria on the catalytic activity for the supported copper catalysts.

Furthermore, It is necessary to examine catalytic performance of the catalysts under the presence of H₂O and CO₂ considering the actual composition of hydrogen-rich streams. The CuO/CeO₂(spheres) catalyst was selected to test its catalytic performance using a simulated reformate streams. As demonstrated in Figure S8 (SI), it is evident that the addition of 10% H₂O and 15% CO₂ has a negative effect on the catalytic activity between 115 and 155 °C.

4. Mechanistic considerations of structure-activity synergy

4.1. Crystallite size, BET surface area and oxygen vacancy

The structural and morphological characterizations show that the smaller crystallite size of ceria exhibit a larger BET surface area. The order of BET surface areas, spheres > spindles > rods > octahedrons > cubes, is the exact opposite of the order of the corresponding mean crystallite sizes. The lattice relaxation was induced by the smaller particle size of CeO₂ when the crystallite size was smaller than 10 nm (spheres). This correlates well with the reduction of Ce⁴⁺ upon decreasing crystallite size (see Table 1). It is evident that the Ce³⁺ proportion decreases with the increase of crystallite size, and the trend of which reduces gradually when the crystallite size was larger than 10 nm. The results were in a good agreement with the report of Zhou and Huebner [51].

The order of reactivity for the oxygen vacancy formation is {110} > {100} > {111} [52,53]. However, as seen in Table 3, the order of corresponding concentration of oxygen vacancies is spheres > spindles > rods = cubes > octahedrons. It can be observed that the combination of {111} and {002} on ceria is more favorable for the formation of oxygen vacancies due to the creation of more defects at

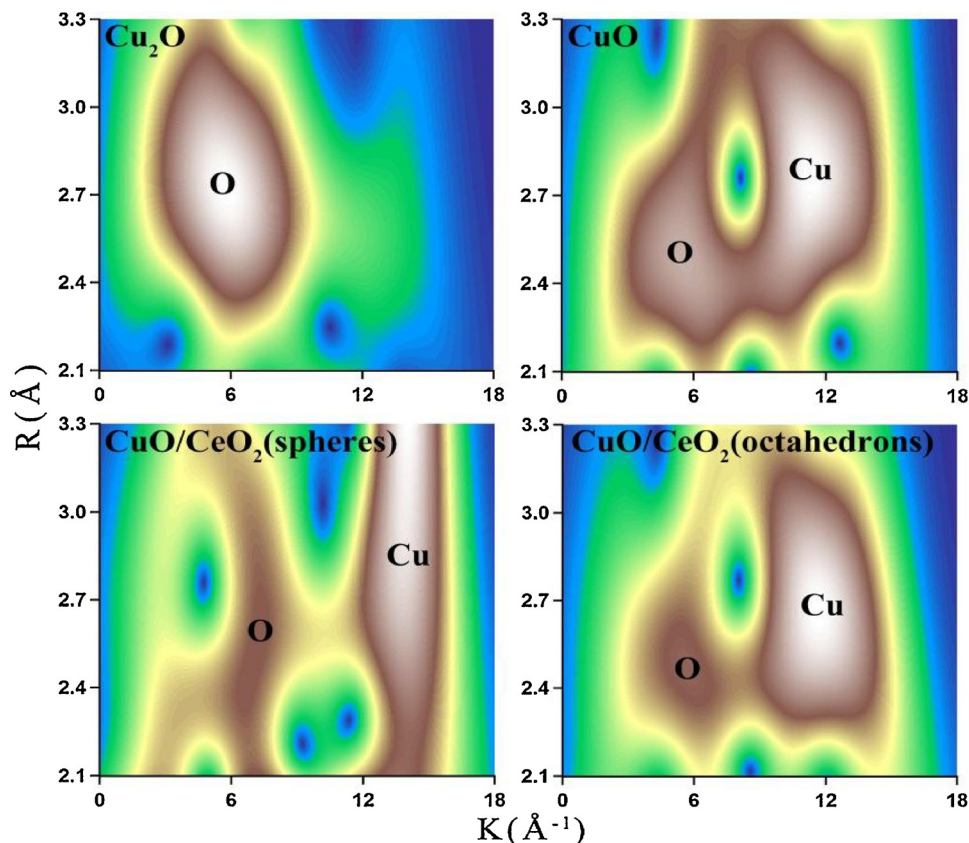


Fig. 9. Wavelet transform spectra of CuO/CeO₂(spheres) and CuO/CeO₂(octahedrons) catalysts (The wavelet transform was obtained through the EXAFS blue frame area).

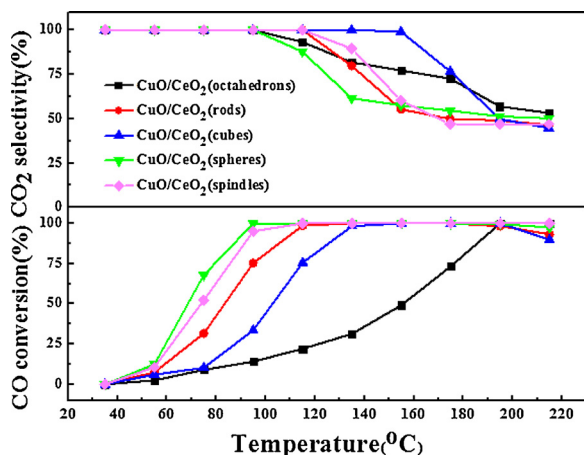


Fig. 10. CO conversion and CO₂ selectivity over the CuO/CeO₂ catalysts with different support shapes.

the intersection sites between {111} and {002} facets. In addition, the copper nanoparticles anchored on ceria {111} facets show a slightly higher oxidation state, whereas those supported on {002} facets are in a slightly lower oxidation state. Furthermore, the intersection sites of {111} and {002} facets can easily generate oxygen vacancies as a result of favorable electron transport. It is known that oxygen vacancies are the key component in the process of oxygen storage and play a central role in oxygen activation in CO-PROX reaction because oxygen vacancies are beneficial to electron capture and transfer, and promote the mobility of oxygen. These vacancies facilitate the oxygen molecules to transform into active oxygen species that participate in the CO oxidation [26].

The highest concentration of oxygen vacancies was found in the CuO/CeO₂(spheres). A large number of oxygen vacancies under stoichiometric CeO_{2-x} can improve oxygen storage capacity (OSC) of ceria, which is closely correlated with catalytic performance of ceria-based catalysts. The OSC increases with increasing the exposure of the more reducible {100} and {110} planes, which exhibits the order of nanocubes > nanorods > nanopolyhedra [18]. By removing an open 2 coordinate oxygen at the intersection between {100} and {111} facets, stable oxygen vacancies with the smallest formation energy of vacancy can be created [18]. The exposed planes of CeO₂ spheres and spindles, {111} and {002} crystal planes, are favorable for the formation of stable oxygen vacancies (see Fig. 11), leading to the catalytic activity of these samples.

Moreover, the oxygen vacancies can activate oxygen molecule and

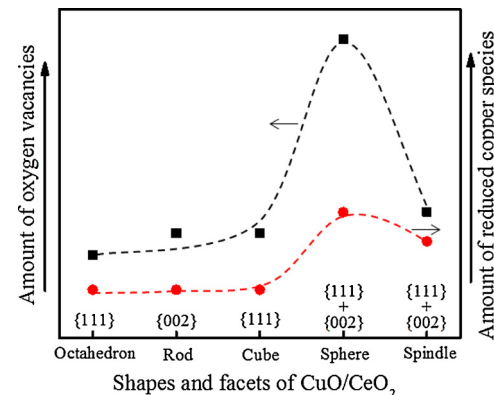


Fig. 11. Plots of the amount of oxygen vacancies and reduced copper species for the CuO/CeO₂ catalysts with different support shapes.

transform it into lattice oxygen which participates in CO oxidation reaction. An increase in oxygen vacancies improves the transformation of molecular oxygen to lattice oxygen.

4.2. Interaction sites and their effect on the reduction of copper species

The combined results from UV-vis and H₂-TPR analyses show that the interaction sites between copper oxides and ceria exhibits the order of spheres > spindles > rods > cubes > octahedrons. The interaction can generate synergistic effect between the two oxides to improve the catalytic activity for the PROX reaction. Indeed, as shown in Fig. 10, the synergistic effect is in a good agreement with the order of catalytic activity.

The amount of reduced copper species on the surface of CuO/CeO₂ catalysts is directly related with the exposed planes of CeO₂. Jacobsen et al. [54] reported that the CuO interacted with CeO₂ exposing {100} faces is more active for CO oxidation than the one in contact with CeO₂ {111} facets because the {100} faces facilitate the change of CuO in terms of the valence. The increase in the reduced copper species on the surface of the CuO/CeO₂(spheres) and CuO/CeO₂(spindles) catalysts leads to more oxygen vacancies than the other samples. Such vacancies could assist the change of the valence for the copper species. As shown in Fig. 11, there is a clear trend that the amount of reduced copper species increases with the concentration of oxygen vacancies.

4.3. Assessment of surface adsorption and oxygen vacancy based DFT calculation

It is evident that engineering the shapes of CeO₂ support at nanoscale essentially leads to exposing specific facets related to the catalytic reaction. To the best of our knowledge, this high level of intrinsic activity in CeO₂ nanosphere consisting of {111} and {002} facets appears new in terms of maneuvering the concentration of oxygen vacancies or Ce³⁺. This facet-directed synergy was also supported by the results from DFT calculation based on a Ce₆₀O₁₂₀ cluster model (Scheme S1). Note that this work has focused on comparing the energy of CO adsorption energy and oxygen vacancy formation energy of different CeO₂ facets to obtain their trends without considering Hubbard parameter correction describing the Ce 4f electron localization effects, and Hubbard parameter would affect the values of above mentioned energies but not the trends (see Table S2) [55].

The DFT calculation was performed for CO adsorption on the {111}, {002} facets and their intersection of CeO₂ using pristine Ce₆₀O₁₂₀ cluster model. The resulting CO adsorption energy (Fig. 12) revealed an intermediate value for the adsorption at the intersection site between {111} and {002} facets. On such sites, CO would readily adsorb or desorb, thus facilitating CO-PROX reaction.

Oxygen vacancy formation was also considered for CeO₂ {111}, {002} and the intersection site between {111} and {002} facets. Fig. 13

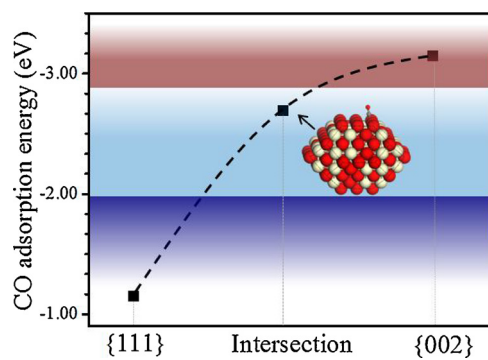


Fig. 12. DFT-calculated adsorption energy for molecularly adsorbed CO on {111}, {002} facets and their intersection sites of a Ce₆₀O₁₂₀ cluster obtained.

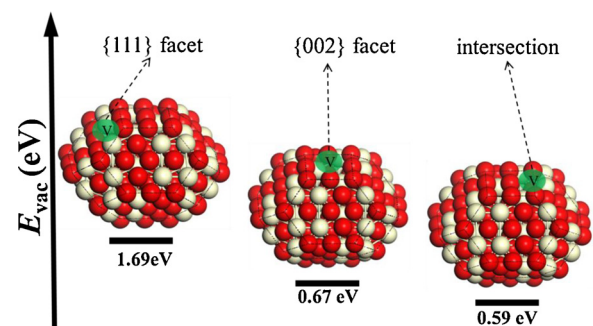


Fig. 13. Models of the optimized geometries of Ce₆₀O₁₁₉ with an oxygen vacancy in the highlighted positions: {111}, {002} facets and their intersection, and values of oxygen vacancy formation energy (E_{vac}) below models. (Color code: O in red, Ce in grey, oxygen vacancy in highlighted circle labeled "V").

shows the optimized geometries of Ce₆₀O₁₁₉ cluster with an oxygen vacancy obtained by removing O atoms at the highlighted position labeled "V" from pristine Ce₆₀O₁₂₀ cluster, and the corresponding vacancy formation energy (E_{vac}). The E_{vac} values are 1.69 eV for {111} facet, 0.67 eV for {002} facet and 0.59 eV for their intersection site, respectively, exhibiting the order of {111} > {002} > {111}/{002} intersection site. Apparently, the most oxygen vacancies are found at the {111}/{002} intersection site, whereas the least at the {111} facet. The oxygen vacancy is known to create two Ce³⁺ cations by transferring two electrons to two Ce⁴⁺ cations, which allows easier adsorption and desorption of active oxygen species, thus promoting oxygen adsorption to form active peroxy species at CeO₂ surfaces and/or interfaces in complex materials, such as CuO/CeO₂ catalyst [46,56,57]. The combination of the theoretical and the experimental results reveals the origin of the high activity by pinning the formation of oxygen vacancy or Ce³⁺ ions to intersection of CeO₂ crystal planes.

5. Conclusions

Taken together, the results have demonstrated the shape controllability of the hydrothermal-impregnation synthesis of CuO/CeO₂ nanocatalysts and its synergistic impact on the catalytic activity for CO-PROX. This is evidenced by the finding that CuO/CeO₂(spheres) and CuO/CeO₂(spindles) with exposed {111} and {002} crystal planes of ceria exhibit not only a much lower temperature for CO conversion but also a wider temperature window for complete CO conversion than those of the other shapes. This finding, together with DFT calculation results showing the enrichment of oxygen vacancies at the intersection sites of {111} and {002} facets, pins the origin of the high catalytic activity to the intersection of the nanocrystal planes. The high concentration of Ce³⁺ defects and oxygen vacancies in ceria induces the formation of Cu⁺ during the process of $\text{Cu}^{2+} + \text{Ce}^{3+} \rightarrow \text{Cu}^{1+} + \text{Ce}^{4+}$ and facilitates PROX reaction. These findings suggest that the catalysts can be manipulated by predominately exposing {111} and {002} facets to alter the structure at the interaction between the two oxides, which has significant implications for the design and preparation of highly-active catalysts.

Acknowledgements

The authors would like to acknowledge support from the National Natural Science Foundation of China (grant no. 21466024), the National Science Foundation of Inner Mongolia (grant no. 2018MS02020 and 2018BS02008), and the National Science Foundation (CHE 1566283).

Appendix A. Supplementary data

Supplementary material related to this article can be found, in the

online version, at doi:<https://doi.org/10.1016/j.apcatb.2018.08.066>.

References

- [1] A. Davó-Quiñonero, D. Lozano-Castelló, A. Bueno-López, *Appl. Catal. B: Environ.* 217 (2017) 459–465.
- [2] Y. Xie, M. Gao, H. Zhang, S. Zeng, X. Zhao, Y. Zhao, H. Su, J. Song, X. Li, Q. Jia, *Int. J. Hydrogen Energy* 41 (2016) 21979–21989.
- [3] W.B. Kim, T. Voitl, G.J. Rodriguez-Rivera, S.T. Evans, J.A. Dumesic, *Angew. Chem. Int. Ed.* 44 (2005) 778–782.
- [4] V.V. Dutov, G.V. Mamontov, V.I. Zaikovskii, L.F. Liotta, O.V. Vodyankina, *Appl. Catal. B: Environ.* 221 (2018) 598–609.
- [5] S. Alayoglu, A.U. Nilekar, M. Mavrikakis, B. Eichhorn, *Nat. Mater.* 7 (2008) 333–338.
- [6] F. Xu, K. Mudiyanseilage, A.E. Baber, M. Soldemo, J. Weissenrieder, M.G. White, D.J. Stacchiola, *J. Phys. Chem. C* 118 (2014) 15902–15909.
- [7] M. Gao, Y. Zhao, S. Zeng, H. Su, *Catal. Commun.* 72 (2015) 105–110.
- [8] Y. Xia, Y. Xiong, B. Lim, S.E. Skrabalak, *Angew. Chem. Int. Ed.* 48 (2009) 60–103.
- [9] G. Yi, H. Yang, B. Li, H. Lin, K.-i. Tanaka, Y. Yuan, *Catal. Today* 157 (2010) 83–88.
- [10] S. Chang, M. Li, Q. Hua, L. Zhang, Y. Ma, B. Ye, W. Huang, *J. Catal.* 293 (2012) 195–204.
- [11] X. Guo, R. Zhou, *Catal. Sci. Technol.* 6 (2016) 3862–3871.
- [12] W. Wang, W. Yu, P. Du, H. Xu, Z. Jin, R. Si, C. Ma, S. Shi, C. Jia, C. Yan, *ACS Catal.* 7 (2017) 1313–1329.
- [13] S. Wang, L. Zhao, W. Wang, Y. Zhao, G. Zhang, X. Ma, J. Gong, *Nanoscale* 5 (2013) 5582–5588.
- [14] F. Wang, W. Li, X. Feng, D. Liu, Y. Zhang, *Chem. Sci.* 7 (2016) 1867–1873.
- [15] T. Caputo, L. Lisi, R. Pirone, G. Russo, *Appl. Catal. A Gen.* 348 (2008) 42–53.
- [16] V. Gianvito, C. Sara, K. Frank, T. Alessandro, P.-R. Javier, *Angew. Chem. Int. Ed.* 126 (2014) 12265–12268.
- [17] E.W. Zhao, H. Zheng, R. Zhou, H.E. Hagelin-Weaver, C.R. Bowers, *Angew. Chem.* 54 (2015) 14270–14275.
- [18] A. Trovarelli, J. Llorca, *ACS Catal.* 7 (2017) 4716–4735.
- [19] A. Trovarelli, *Catalysis by Ceria and Related Materials*, Imperial College Press, London, 2002.
- [20] J. Kullgren, K. Hermansson, P. Broqvist, *J. Phys. Chem. Lett.* 4 (2013) 604–608.
- [21] N.K. Renuka, N. Harsha, T. Divya, *RSC Adv.* 5 (2015) 38837–38841.
- [22] K.S.W. Sing, D.H. Everett, R.A.W. Haul, L. Moscou, R.A. Pierotti, J. Rouquérol, T. Siemieniewska, *Pure Appl. Chem.* 57 (1985) 603–619.
- [23] L. Cheng, Y. Men, J. Wang, H. Wang, W. An, Y. Wang, Z. Duan, J. Liu, *Appl. Catal. B: Environ.* 204 (2017) 374–384.
- [24] Z. Wu, M. Li, J. Howe, H. Meyer, S. Overbury, *Langmuir* 26 (2010) 16595–16606.
- [25] T. Désaunay, G. Bonura, V. Chiodo, S. Freni, J.P. Couzinié, J. Bourgon, A. Ringuedé, F. Labat, C. Adamo, M. Cassir, *J. Catal.* 297 (2013) 193–201.
- [26] S. Chen, L. Li, W. Hu, X. Huang, Q. Li, Y. Xu, Y. Zuo, G. Li, *ACS Appl. Mater. & Inter.* 7 (2015) 22999–23007.
- [27] A.B. Dongil, B. Bachiller-Baeza, E. Castillejos, N. Escalona, A. Guerrero-Ruiz, I. Rodríguez-Ramos, *Catal. Sci. Technol.* 6 (2016) 6118–6127.
- [28] X. Guo, J. Li, R. Zhou, *Fuel* 163 (2016) 56–64.
- [29] Z. Wang, Z. Qu, X. Quan, Z. Li, H. Wang, R. Fan, *Appl. Catal. B: Environ.* 134–135 (2013) 153–166.
- [30] J. Li, Y. Han, Y. Zhu, R. Zhou, *Appl. Catal. B: Environ.* 108–109 (2011) 72–80.
- [31] F. Wang, R. Büchel, A. Savitsky, M. Zalibera, D. Widmann, S.E. Pratsinis, W. Lubitz, F. Schüth, *ACS Catal.* 7 (2017) 4716–4735.
- [32] A. Elmhamdi, R. Castañeda, A. Kubacka, L. Pascual, K. Nahdi, A. Martínez-Arias, *Appl. Catal. B: Environ.* 188 (2016) 292–304.
- [33] G. Avgouropoulos, T. Ioannides, *Appl. Catal. A Gen.* 244 (2003) 155–167.
- [34] W. Liu, M. Flytzanistephopoulos, *J. Catal.* 153 (1995) 304–316.
- [35] S. Zeng, Y. Wang, S. Ding, J.J.H.B. Sattler, E. Borodina, L. Zhang, B.M. Weckhuysen, H. Su, *J. Power Source* 256 (2014) 301–311.
- [36] S. Rico-Francés, E.O. Jardim, T.A. Wezendonk, F. Kapteijn, J. Gascon, A. Sepúlveda-Escribano, E.V. Ramos-Fernandez, *Appl. Catal. B: Environ.* 180 (2016) 169–178.
- [37] S. Zeng, T. Chen, K. Liu, H. Su, *Catal. Commun.* 45 (2014) 16–20.
- [38] V. Petrovsky, B.P. Gorman, H.U. Anderson, T. Petrovsky, *J. Appl. Phys.* 90 (2001) 2517–2521.
- [39] G.-W. Li, L. Hong, M.-S. Tong, H.-H. Deng, X.-H. Xia, W. Chen, *Anal. Methods* 7 (2015) 1924–1928.
- [40] M.H. Groothaert, J.A. van Bokhoven, A.A. Battiston, B.M. Weckhuysen, R.A. Schoonheydt, *J. Am. Chem. Soc.* 125 (2003) 7629–7640.
- [41] G. Zhou, Y. Yao, X. Zhao, X. Liu, B. Sun, A. Zhou, *RSC Adv.* 6 (2016) 59370–59374.
- [42] T.R. Reina, S. Ivanova, O.H. Laguna, M.A. Centeno, J.A. Odriozola, *Appl. Catal. B: Environ.* 197 (2016) 62–72.
- [43] C.T. Campbell, *Nat. Chem.* 4 (2012) 597–598.
- [44] A. Bruijx, J.A. Rodriguez, P.J. Ramírez, S.D. Senanayake, J. Evans, J.B. Park, D. Stacchiola, P. Liu, J. Hrbek, F. Illas, *J. Am. Chem. Soc.* 134 (2012) 8968–8974.
- [45] Y. Cui, W. Dai, *Catal. Sci. Technol.* 6 (2016) 7752–7762.
- [46] M. Zabilskiy, P. Djinovic, E. Tchernychova, O.P. Tkachenko, L.M. Kustov, A. Pintar, *ACS Catal.* 5 (2015) 5357–5365.
- [47] S.P. Wang, T.Y. Zhang, Y. Su, S.R. Wang, S.M. Zhang, B.L. Zhu, S.H. Wu, *Catal. Lett.* 121 (2008) 70–76.
- [48] C.G. Maciel, Td.F. Silva, L.P.R. Profeti, E.M. Assaf, J.M. Assaf, *Appl. Catal. A* 431–432 (2012) 25–32.
- [49] A. Martínez-Arias, M. Fernández-García, J. Soria, J.C. Conesa, *J. Catal.* 182 (1999) 367–377.
- [50] W. Liu, A. Sarofim, M. Flytzani-Stephanopoulos, *Chem. Eng. Sci.* 49 (1994) 4871–4888.
- [51] X.D. Zhou, W. Huebner, *Appl. Phys. Lett.* 79 (2001) 3512–3514.
- [52] T.X.T. Sayle, S.C. Parker, C.R.A. Catlow, *Surf. Sci.* 316 (1994) 329–336.
- [53] J.C. Conesa, *Surf. Sci.* 339 (1995) 337–352.
- [54] S.N. Jacobsen, U. Helmersson, R. Erlandsson, B. Skärman, L.R. Wallenberg, *Surf. Sci.* 429 (1999) 22–33.
- [55] M. Huang, S. Fabris, *J. Phys. Chem. C* 112 (2008) 8643–8648.
- [56] A. Migani, G.N. Vayssilov, S.T. Bromley, F. Illas, K.M. Neyman, *J. Mater. Chem.* 20 (2010) 10535–10546.
- [57] A.D. Mayernick, M.J. Janik, *J. Phys. Chem. C* 112 (2008) 14955–14964.